ROYAL SOCIETY
OF CHEMISTRY

PAPER

Check for updates

Modulation of vibronic transitions in chlorophyll *a* through strong light–matter coupling

Rebecca M. Gracia, [iD] [ab] Gabriel J. Russo, [iD] [a] Seongje Park,[ab] Lilia Kinziabulatova[ab] and Minjung Son [iD] ⋆[ab]

Strong coupling between molecular electronic transitions and the electromagnetic field of an optical resonator gives rise to hybrid light–matter states known as exciton–polaritons. Polariton states exhibit energies and photophysical properties distinct from their unhybridized molecular counterparts, making exciton–polaritons a powerful platform for engineering photophysical processes in molecular materials. In this work, we demonstrate strong light–matter coupling between a confined photon mode in a metallic Fabry–Pérot microcavity and electronic transitions of chlorophyll *a* (Chl *a*), the primary light-harvesting chromophore in natural photosynthesis. In addition to its strong absorption, Chl *a* features prominent vibronic structure in its absorption spectrum, making it a compelling model system for exploring how vibronic transitions are influenced by cavity coupling. Angle-dependent reflection spectra clearly resolve upper- (UP), middle- (MP), and lower-polariton (LP) branches, indicating that multiple vibronic sub-levels of the Q_y state of Chl *a* contribute to the light–matter coupling in the system, which had not been resolved in previous studies. Furthermore, the narrowing of the LP peak width suggests that strong light–matter interaction can suppress the energetic disorder present in the embedded Chl molecules. These findings present promising opportunities for tailoring vibronic excited-state manifolds and associated relaxation pathways in light-harvesting systems *via* cavity-mediated interactions.

[a] *Department of Chemistry, Boston University, 590 Commonwealth Avenue, Boston, MA 02215, USA. E-mail: mson@bu.edu*
[b] *Boston University Photonics Center, 8 Saint Mary's Street, Boston, MA 02215, USA*

Dr Minjung Son is the David R. Dalton Career Development Assistant Professor of Chemistry at Boston University. She received her BS and MS in Chemistry from Yonsei University and earned her PhD at MIT as a Robert T. Haslam Presidential Fellow, developing ultrabroadband two-dimensional electronic spectroscopy to uncover light-harvesting mechanisms in plants. As a postdoctoral researcher at the University of Wisconsin–Madison, she explored energy-flow

Minjung Son

pathways in exciton–polaritonic systems. Since founding her group in 2023, she has combined ultrafast spectroscopy, microscopy, materials science, photonics, and biophysics to investigate spatiotemporal photophysics in complex molecular and polaritonic systems.

Introduction

Strong coupling between light modes confined in an optical resonator and resonant electronic transitions of molecules results in a hybrid light–matter state known as exciton–polaritons.[1–7] Exciton–polaritons exhibit energy landscapes and photophysical properties that are distinct from those of the bare molecules. The energy levels of polariton states are shifted relative to the original molecular transitions due to what is known as Rabi splitting, a hallmark of strong light–matter coupling. The magnitude of Rabi splitting can be tailored in a straightforward manner by varying parameters such as the concentration and orientation of the embedded molecules, providing a versatile means of engineering their excited-state energy landscape. Furthermore, due to their partial photonic character, polariton states display a dispersive energy landscape in which the energy levels are sensitive to the angle, or the in-plane wavevector, of spectroscopic measurements, a feature that is absent in purely molecular systems. Leveraging these unique attributes of light–matter hybridization, exciton–polaritons are increasingly being used as a platform in which the photophysical, optical, and electronic properties of molecular systems can be systematically modified. These altered properties have been shown to enable a plethora of otherwise challenging processes, including enhanced intermolecular

energy transfer over an extended distance,[8–13] modulation of chemical reactivity and conductivity,[14–16] and reduced energy losses in photovoltaics.[17–19]

Achieving strong light–matter coupling requires molecular transitions with large oscillator strengths and narrow absorption linewidths. Porphyrin derivatives represent a prominent class of molecules that satisfy these conditions and are utilized as important building blocks in both natural and artificial light-harvesting systems. As described by the Gouterman four-orbital model, these molecules exhibit two sharp, intense absorption bands, commonly referred to as the Soret and Q bands, in the blue and red regions of the visible spectrum.[20] Indeed, strong light–matter coupling has been demonstrated and extensively studied in a variety of porphyrin molecules and their derivatives placed in optical microcavities,[21–26] including the very first report of organic exciton–polaritons by Lidzey *et al.*[27]

An example of particular importance in this class of molecules is chlorophyll (Chl), which serves as the primary light-harvesting pigment in oxygenic photosynthesis.[28] Along with its biological importance and strong absorptivity, the well-defined and relatively intense vibronic features in its absorption spectrum make Chl an intriguing model system for investigating the impact of light–matter coupling on vibronic transitions. Light–matter coupling involving Chl *a* (Fig. 1a), the most abundant form of Chl, has been demonstrated almost exclusively in plasmonic platforms. Plasmonic nanocavities with various geometries, such as gold nanoparticles, nanocubes, and nanorings, have been reported to allow strong coupling between the Q band of Chl *a* and the localized surface plasmon of the gold nanostructures.[29–31] While these studies reported strong light–matter coupling strengths of approximately 100 meV, based on a Rabi splitting energy of ∼200 meV, only two polariton branches were resolved, namely the upper- (UP) and lower polariton (LP), with no contribution from higher-lying vibronic states observed.

In this work, we report the formation of exciton–polaritons arising from strong interactions between electronic transitions of Chl *a* and a photon mode confined within a metallic Fabry–Pérot microcavity. Notably, we observe a previously unresolved middle polariton (MP) branch in addition to the UP and LP states, indicating that multiple vibronic levels of the Q band not only interact simultaneously with the cavity photon mode but also hybridize with one another. We demonstrate that the spectral features, such as relative peak intensities and line-widths, can be further fine-tuned as a function of cavity parameters, which may lead to a new strategy toward precise and systematic control of the vibronic excited-state manifolds of molecular materials.

Experimental

Preparation of Chl *a* thin film layers

Chl *a* powder extracted from spinach was purchased from Millipore Sigma and used without further purification. The powder was dissolved in toluene to create a stock solution with a concentration of 2.5 mg mL^{-1}. Thin film layers of Chl *a* were prepared by mixing the stock solution with poly(methyl methacrylate) (PMMA) polymer (Kayaku Advanced Materials) at volume fractions of 15%, 25%, and 35% Chl *a*. Thin films were produced by drop-casting these mixtures onto a quartz cover slip (Electron Microscopy Sciences; for control samples) or a silver-coated cover slip (for microcavities) and dried overnight. The thickness of the resulting Chl *a* layers was characterized with an atomic force microscope (MFP-3D-BIO, Asylum Research, Oxford Instruments) prior to microcavity fabrication.

Fabrication of Fabry–Pérot microcavities

Silver-coated reflectors were prepared by thermal evaporation of 30 nm silver on quartz cover slips described above using a thermal evaporator (Covap, Angstrom Engineering). The silver
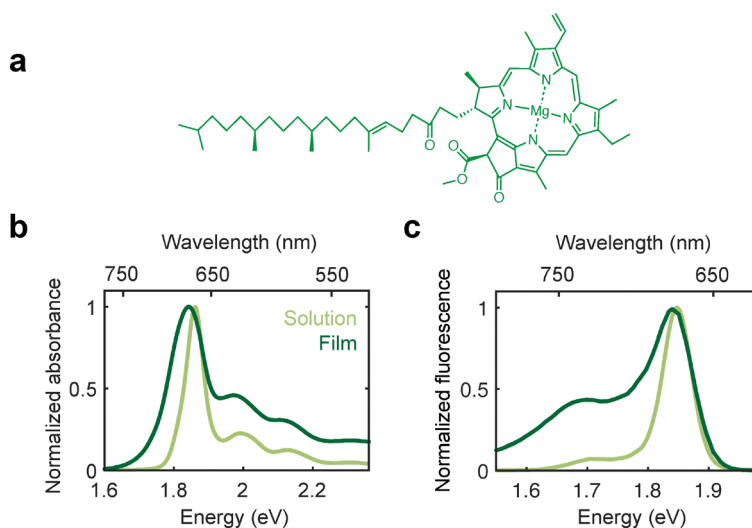
Fig. 1 (a) Chemical structure of Chl *a*. (b) Normalized steady-state absorption spectra of Chl *a* dissolved in toluene (light green) and in a film (dark green), zoomed in onto the Q-band region. (c) Normalized fluorescence emission spectra of Chl *a* dissolved in toluene (light green) and in a film (dark green) measured upon excitation at 420 nm.

pellets were purchased from Kurt J. Lesker. Prior to silver deposition, the cover slips were cleaned through three successive rounds of sonication in acetone for 15 minutes each, followed by two rounds of soaking in 2-propanol at 80 °C for 20 minutes each. Both solvents were purchased from Millipore Sigma and filtered through membrane filters with a pore size of 0.2 mm made of polytetrafluoroethylene (PTFE) and nylon (Fisher Scientific) for acetone and 2-propanol, respectively, prior to the cleaning procedure. The Chl a/PMMA mixture described above was drop-cast onto a silver-coated substrate and dried overnight. Closed Fabry–Pérot microcavities were subsequently formed by thermally evaporating a second layer of 30 nm silver on top.

Spectroscopic characterizations

Steady-state absorption spectra of Chl a solution as well as film were measured with a Cary 5000 UV-vis-NIR spectrophotometer (Agilent). The fluorescence emission spectrum of the solution-phase sample was measured with a Cary Eclipse fluorimeter (Agilent). A Tecan Spark multimode plate reader was used to measure the fluorescence emission spectra of solid-state samples. All solutions were measured in a quartz cuvette.

Angle-dependent reflection spectra of the microcavities were measured using a variable-angle spectroscopic ellipsometer (V-VASE, J. A. Woollam). A focused white light beam with transverse electric (TE) polarization (spot size of 0.2 mm) was directed at the sample, and the reflected light was collected. Measurements were performed at incident angles ranging from 20° to 70°, in increments of 5°, using a motorized goniometer.

Modeling of the reflection spectra

Coupled oscillator modeling was used to extract quantitative parameters about the system, such as the magnitude of light–matter coupling, energy level of each polariton state, and the photon dispersion curve.[32] In this model, the angle-dependent cavity photon mode $E_c(\theta)$ is given by $E_c(\theta) = E_c(0)/\sqrt{1 - (\sin\theta/n_{eff})^2}$, where $E_c(0)$ is the photon energy at normal incidence ($\theta = 0°$) and n_{eff} is the effective refractive index. In this work, a fixed n_{eff} value of 1.92 was used. A 3×3 Hamiltonian was constructed using the photon energy, $E_c(\theta)$, and two exciton energies, E_{0-0} and E_{0-1}, as diagonal elements:

$$\begin{pmatrix} E_c(\theta) & g_1 & g_2 \\ g_1 & E_{0-0} & 0 \\ g_2 & 0 & E_{0-1} \end{pmatrix} \begin{pmatrix} \alpha_c \\ \alpha_{0-0} \\ \alpha_{0-1} \end{pmatrix} = E \begin{pmatrix} \alpha_c \\ \alpha_{0-0} \\ \alpha_{0-1} \end{pmatrix} \quad (1)$$

where E_{0-0} and E_{0-1} are the exciton energies of the $Q_y(0-0)$ and $Q_y(0-1)$ bands of Chl a, respectively, determined from steady-state absorption spectra (Fig. 1b). The off-diagonal elements, g_1 and g_2, are the light–matter coupling strengths between the cavity photon mode and the $Q_y(0-0)$ and $Q_y(0-1)$ bands of Chl a, respectively. Diagonalization of the Hamiltonian matrix shown above yields the energy levels of the resulting UP, MP, and LP eigenstates. α_c, α_{0-0}, and α_{0-1} are the Hopfield coefficients,

which are parameters that represent the photonic, $Q_y(0-0)$, and $Q_y(0-1)$ contributions, respectively, to each polariton state. $E_c(0)$, g_1, and g_2 were iteratively varied until the polariton eigenstate energies at all angles ($\theta = 20-70°$) matched the peak positions identified in the experimental angle-dependent reflection spectra. The experimental peak positions were determined by locating local minima in the second derivative of each reflection spectrum. Because the coupling strength scales with the transition dipole moment, we restricted g_2 to only vary between 65–70% of g_1, based on the absorption peak ratio $A_{0-1}/A_{0-0} = 0.458$ (where A_{0-1} and A_{0-0} represent the absorbance of Chl a at the $Q_y(0-1)$ and $Q_y(0-0)$ peaks, respectively).

Results and discussions

Spectroscopic characterization of Chl a thin films

Fig. 1a and b illustrates the chemical structure of Chl a (Fig. 1a) and its steady-state absorption (Fig. 1b) spectra in toluene solution and in a film prepared by drop-casting the solution on a glass cover slip. Spectral features in the absorption spectra are consistent with the electronic structure of Chl a predicted by Gouterman's model;[20] two intense absorption bands appear at 2.86 (solution) and 2.84 (film) eV and 1.86 (solution) and 1.84 (film) eV, known as the Soret and $Q_y(0-0)$ bands, respectively (see Fig. S1 for absorption spectra plotted over an extended wavelength range including the Soret band).[33] Additional peaks with weaker absorbance are observed between the two bands, which are attributed to vibronic transitions of the Q_y state and/or the higher-lying Q_x state, although the exact assignment remains undetermined.[33,34] The absorption peaks of the film are redshifted as well as broadened compared to those in solution, indicative of the presence of non-negligible intermolecular interactions in the film and in agreement with previously reported absorption spectra of Chl a in the solid state.[35,36] The spectral features did not vary with Chl a content in the films, suggesting that the extent of intermolecular interactions remained identical (Fig. S2). Consistent with the spectral changes observed in the absorption spectra, the fluorescence emission spectrum of the Chl a film (Fig. 1c) is also partly redshifted and substantially broadened, further suggesting the presence of interactions between the Chl a molecules within the film. Moreover, the red emission band at ~1.7 eV gains a significant intensity in the solid state. A similar phenomenon has been observed in a thin film of chlorin, which shares a largely similar chemical structure to Chl molecules, and attributed to intermolecular interactions.[25]

Light–matter coupling in microcavities

Light–matter coupling was achieved by incorporating the Chl a film into a series of Fabry–Pérot microcavities, fabricated with 30 nm silver mirrors on both sides, as described in the Experimental section. The cavity thickness was chosen to ensure strong spectral overlap between the first photon mode and the $Q_y(0-0)$ transition of Chl a, as determined by transfer matrix method (TMM) simulations (Fig. S3).[37,38] Higher-order

photon modes were not considered, as they occur in the ultraviolet range with large detunings from the Q-band transitions (Fig. S4). The TMM simulations yielded an optimal thickness of approximately 180 nm (Fig. S3), which was achieved experimentally by drop-casting a PMMA layer containing Chl a at a volume fraction of 25%. As illustrated in Fig. 2, we were able to systematically tune the thickness of the active layer by varying the Chl a content in the PMMA matrix. At 15% and 35% Chl a, the resulting active layer thicknesses were 160 nm and 200 nm, corresponding to positively and negatively detuned photon modes relative to the $Q_y(0-0)$ state, respectively, according to the TMM simulations.

The contour maps in Fig. 2 show the angle-dependent reflection spectra of the three microcavities mentioned above. In all cases, we observe pronounced changes in the positions as well as relative intensities of the reflection peaks compared to the absorption spectrum of bare Chl a, highlighting the impact of light–matter coupling in these systems. Unlike in previous studies of Chl a polaritons, where only two polariton branches, *i.e.*, UP and LP, were resolved, our reflection spectra reveal an additional MP branch along with the UP and LP branches. This observation clearly indicates simultaneous coupling of the $Q_y(0-0)$ and the higher-lying vibronic transitions to the cavity photon mode. Additionally, the fluorescence emission spectra of the microcavities further support the modification of the photophysical properties in the presence of light–matter interaction (Fig. S5). Unlike the bare Chl a fluorescence, which exhibits two emission peaks, the microcavities show only a single emission peak. These peaks occur near the LP energies

identified in the reflectance spectra and shift systematically with cavity thickness.

To quantitatively determine the extent of light–matter coupling in each microcavity, we modeled the peak positions of the three polariton branches, UP, MP, and LP, observed in the experimental reflectance spectra using a coupled oscillator model as described in the Experimental section. In our model, only the energy levels of the $Q_y(0-0)$ state and the first vibronic band, $Q_y(0-1)$, were included as exciton energies (E_{0-0} = 1.84 eV, E_{0-1} = 1.98 eV from the film absorption spectrum in Fig. 1b). A fourth peak, associated with contributions from the (0–2) band at 2.13 eV (Fig. 1b), is predicted by TMM simulations (Fig. S6) and observed in some spectra. However, this peak could not be reliably resolved, particularly at small angles, where the exciton energy is significantly detuned from the photon mode.

Table 1 summarizes the best-fit parameters obtained from the coupled oscillator model, including the two coupling strengths, g_1 and g_2, as well as the photon energy at normal incidence, $E_c(0)$. The resultant energy levels of the UP, MP, LP states, along with the corresponding photon dispersion curve, are displayed and labeled in Fig. 2 with black and orange solid lines. Consistent with the predictions from the TMM simulations (Fig. S3), the photon mode is positively detuned relative to the $Q_y(0-0)$ transition at all angles in the microcavity with a 160 nm Chl a layer and negatively detuned in the 200 nm cavity. The 180 nm cavity exhibits minimal detuning with the photon dispersion curve crossing the $Q_y(0-0)$ energy at 38°. The magnitude of g_1 grows from 105 ± 6 to 124 ± 8 to 136 ± 8 meV as
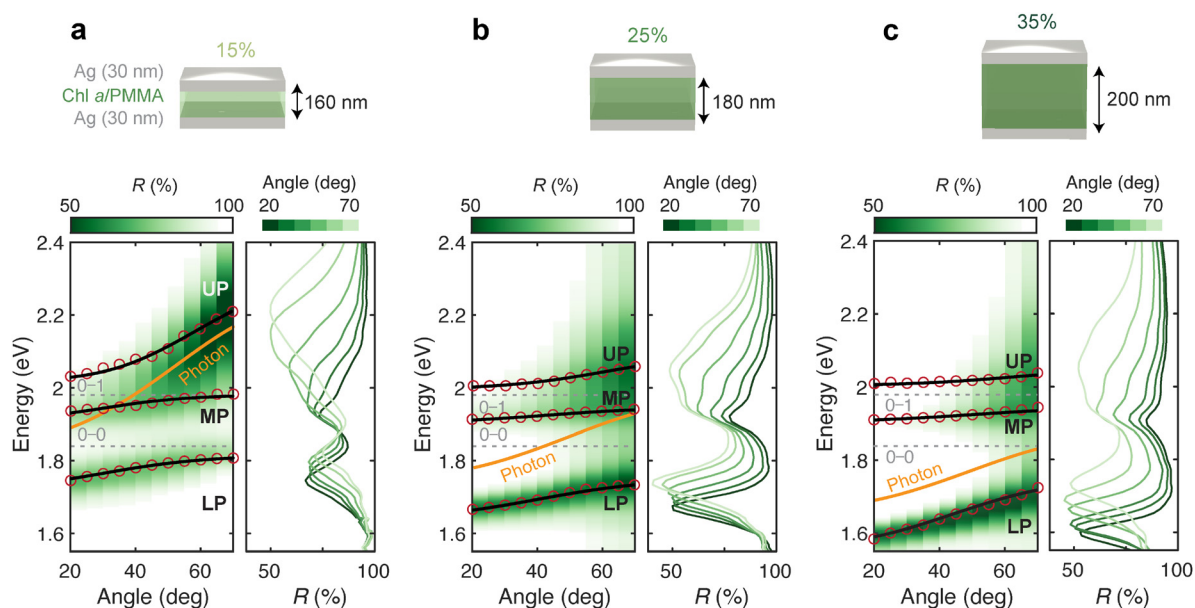
Fig. 2 Angle-dependent reflection spectra (*R*: reflectance) of the microcavity with increasing Chl a layer thickness of 160 nm (a), 180 nm (b), and 200 nm (c), which were obtained by increasing the Chl a content in the active layer from 15% (a) to 25% (b) to 35% (c). Best fit results from coupled oscillator modeling are shown as solid lines; the UP, MP, and LP energies determined from the fit are shown in black, and the photon dispersion curve is shown in orange. Red open circles show the peak positions determined from the second-derivative analysis and used in the coupled oscillator model. The exciton energy levels of the Chl a $Q_y(0-0)$ and (0−1) bands are shown as gray dashed lines. To better illustrate the spectral features, one-dimensional reflection spectra are also shown on the right at incident angles of 20 to 70 degrees in 10 degree increments.

Table 1 Best fit parameters from coupled oscillator model. Error bars report 95% confidence intervals of the fit

| Active layer thickness (nm)	$E_c(0)$ (eV)	g_1 (meV)	g_2 (meV)	g_2/g_1 (%)
160	1.86 ± 0.03	105 ± 6	71 ± 8	68 ± 9
180	1.77 ± 0.04	124 ± 8	81 ± 8	65 ± 8
200	1.67 ± 0.04	136 ± 8	91 ± 9	67 ± 8

the thickness of the Chl a layer increases, reflecting the corresponding increase in the number of molecules participating in the light–matter interaction. Similarly, g_2 values were found to increase from 71 ± 8 to 81 ± 8 to 91 ± 9 meV. The ratio g_2/g_1 was found to be nearly constant at 65–68%, which is consistent with the prediction from the $Q_y(0–1)/Q_y(0–0)$ peak intensity ratio mentioned above.

The observation that the strongest coupling occurs in the negatively detuned microcavity suggests that the number of coupled molecules (N) is the dominant factor governing the extent of light–matter interaction in these systems. In Fig. 3a, we plot the light–matter coupling strengths g_1 and g_2 as a function of the square root of the Chl a content in the active layer. Both exhibit linear scaling, confirming the collective nature of the light–matter interactions, where the coupling strength scales with $\sqrt{N}$.[1,2,39] The energy splitting between the UP and LP states observed in our systems, ranging from 282 to 425 meV, is significantly larger than the values of $\sim$200 meV previously reported in Chl a-based polaritons in

plasmonic cavities even in the presence of detuning[29–31] (Fig. 3b). Although these values cannot be directly compared due to differences in peak assignments and the absence of an MP observed in these earlier works, we attribute this increase in the splitting energy to the large number of molecules coupling to the photon mode, despite the considerably larger mode volume of our Fabry–Pérot microcavities compared to the plasmonic nanocavities.

To gain quantitative insights into the relative photonic and excitonic content of the polariton states, we analyzed the Hopfield coefficients, as shown in Fig. 4. In all three samples, the UP and LP branches are dominated by the exciton mode closest in energy, while having little contribution from the more distant exciton mode. The MP branch reveals strong hybridization between the two excitonic modes, with the photon mode contributing a minor fraction of 25% or less. These results are qualitatively consistent with the trends observed in other systems exhibiting middle polariton branches and suggest that exciton–polaritons can facilitate strong interactions not only between photonic and excitonic modes but also between excitonic – specifically vibronic – states within the molecular energy manifold.[22,40–43] In fact, the MP branch has been proposed to serve as a key mediator of enhanced intermolecular energy transfer observed in polaritonic systems.[9,44]

Finally, we note that the spectral features of the reflectance spectra, including the linewidth and intensity of the peaks, are sensitive to cavity thickness. In the 160 nm cavity, the photon mode is positively detuned relative to the $Q_y(0–0)$ state, resulting in stronger overlap with the (0–1) transition and greater photonic character in the UP branch compared to the lower-lying branches. This leads to enhanced intensity on the high-energy side of the spectrum, particularly at larger angles. In contrast, the LP branch becomes significantly more pronounced in the 180 nm and 200 nm cavities, where the photon mode is more strongly coupled to the $Q_y(0–0)$ band and the LP branch carries the largest photon character. Furthermore, the full-width at half maximum (FWHM) of the LP peak in these two cavities is as narrow as 63 and 70 meV, respectively, considerably smaller than the parent exciton peak width of 128 meV (Fig. 1b and Fig. S7–S9, and Table S1). In contrast, no significant line narrowing was observed for the positively detuned 160 nm cavity, where the LP peak width was only slightly reduced compared to the $Q_y(0–0)$ band (Fig. S10). The pronounced linewidth narrowing observed for the 180 nm and 200 nm cavities can be attributed to the polaron decoupling effect, wherein strong light–matter coupling suppresses energetic disorder by effectively decoupling electronic and nuclear degrees of freedom.[45–48] The observed parabolic dependence of the LP peak width on the exciton fraction (Fig. 5) is in agreement with theoretical predictions of linewidth narrowing in polaritons embedding inhomogeneously broadened excitons.[49,50] Similar non-linear dispersion of the LP width has also been reported in microcavities containing porphyrin-based chromophores.[51,52] Taken together, these observations highlight the potential of exciton–polaritons as a means to
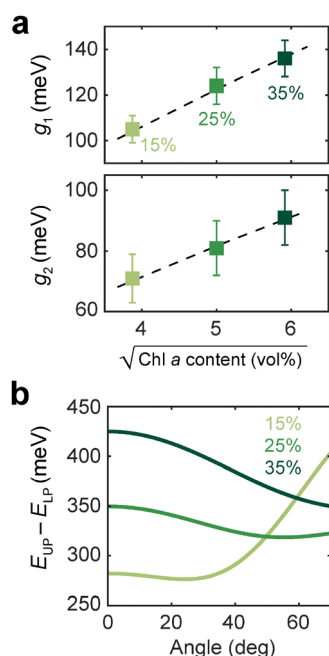

Fig. 3 (a) Light–matter coupling strengths identified in the three microcavities plotted as a function of the square root of Chl a content (top: g_1, bottom: g_2). Dashed lines serve as a guide to the eye, illustrating the linear trend. (b) Plot of the difference between the UP energy (E_{UP}) and LP energy (E_{LP}) in the three microcavities.
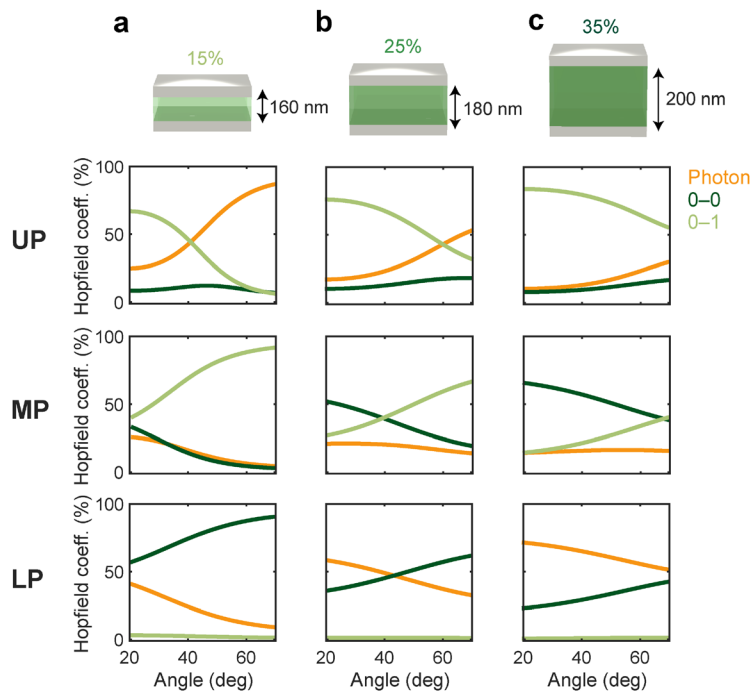
Fig. 4 Hopfield coefficients extracted from coupled oscillator modeling. Each row plots the coefficients for the UP (top), MP (middle), and LP (bottom) states for the three microcavities with Chl *a* layer thickness of 160 nm (a), 180 nm (b), and 200 nm (c). Orange, dark green, and light green curves illustrate the photonic, $Q_y(0-0)$, and $Q_y(0-1)$ character of each state, respectively.
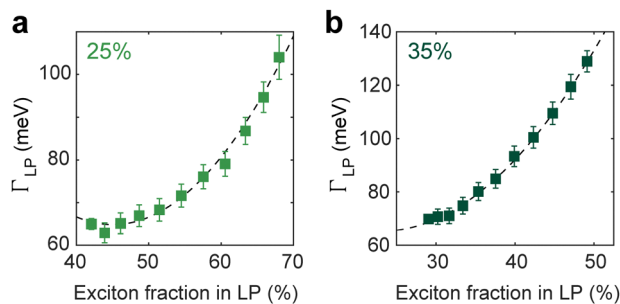
Fig. 5 FWHM of the LP peaks (Γ_{LP}) in the cavities with 25% (a) and 35% (b) Chl *a* content plotted as a function of the exciton fraction in the LP branch, as extracted from the Hopfield coefficients shown in Fig. 4. Dashed lines serve as a guide to the eye, illustrating the parabolic trend. Error bars represent 95% confidence intervals.

enables the resolution of an additional polariton branch, which arises from coupling between the photon mode and higher-lying vibronic states of the Q_y band. The intensity and linewidth of the polaritonic peaks exhibit strong dependence on cavity detuning. Remarkably, we observe substantial motional narrowing of the LP peak, indicative of suppression of excitonic disorder through strong light–matter interaction. These findings represent promising initial steps toward harnessing light–matter coupling to manipulate the energetics and relaxation pathways of light-harvesting chromophores, and ultimately to engineer inter-chromophore energy transfer processes in more complex systems such as photosynthetic antenna proteins or artificial chromophore assemblies toward enhanced functionality.

systematically modulate the vibronic excited-state manifolds of molecular chromophores.

Conclusions

In this work, we demonstrate the formation of exciton–polaritons with Chl *a* embedded in Fabry–Pérot microcavities. The observed UP-LP energy gap of ∼400 meV places our system in the strong coupling regime, underscoring the ability of light–matter interactions to drastically reshape the energy landscape of molecular chromophores without chemical modifications. The combination of a high molecular density within the cavity and the inherently well-defined vibronic structure of Chl *a*

Author contributions

M. S. conceived and supervised the study. R. M. G., G. J. R., and S. P. fabricated the samples. R. M. G., L. K., and M. S. performed optical characterizations and modeling and analyzed data. All authors contributed to the writing and editing of the manuscript.

Conflicts of interest

There are no conflicts to declare.

Data availability

The data supporting this article have been included as part of the SI. Transfer matrix method simulation results, additional absorption and fluorescence spectra, and modeling results. See DOI: **https://doi.org/10.1039/d5tc03240g**.

Acknowledgements

Notes and references

1 T. W. Ebbesen, *Acc. Chem. Res.*, 2016, **49**, 2403–2412.
2 M. Hertzog, M. Wang, J. Mony and K. Börjesson, *Chem. Soc. Rev.*, 2019, **48**, 937–961.
3 R. F. Ribeiro, L. A. Martínez-Martínez, M. Du, J. Campos-Gonzalez-Angulo and J. Yuen-Zhou, *Chem. Sci.*, 2018, **9**, 6325–6339.
4 F. Herrera and J. Owrutsky, *J. Chem. Phys.*, 2020, **152**, 100902.
5 R. Bhuyan, J. Mony, O. Kotov, G. W. Castellanos, J. Gómez Rivas, T. O. Shegai and K. Börjesson, *Chem. Rev.*, 2023, **123**, 10877–10919.
6 S. Dhamija and M. Son, *Chem. Phys. Rev.*, 2024, **5**, 041309.
7 F. Fassioli, K. H. Park, S. E. Bard and G. D. Scholes, *J. Phys. Chem. Lett.*, 2021, **12**, 11444–11459.
8 X. Zhong, T. Chervy, S. Wang, J. George, A. Thomas, J. A. Hutchison, E. Devaux, C. Genet and T. W. Ebbesen, *Angew. Chem., Int. Ed.*, 2016, **55**, 6202–6206.
9 M. Wang, M. Hertzog and K. Börjesson, *Nat. Commun.*, 2021, **12**, 1874.
10 M. Son, Z. T. Armstrong, R. T. Allen, A. Dhavamani, M. S. Arnold and M. T. Zanni, *Nat. Commun.*, 2022, **13**, 7305.
11 D. Timmer, M. Gittinger, T. Quenzel, S. Stephan, Y. Zhang, M. F. Schumacher, A. Lützen, M. Silies, S. Tretiak and J.-H. Zhong, *et al.*, *Nat. Commun.*, 2023, **14**, 8035.
12 A. Cargioli, M. Lednev, L. Lavista, A. Camposeo, A. Sassella, D. Pisignano, A. Tredicucci, F. J. Garcia-Vidal, J. Feist and L. Persano, *Nanophotonics*, 2024, **13**, 2541–2551.
13 K. Georgiou, R. Jayaprakash, A. Othonos and D. G. Lidzey, *Angew. Chem., Int. Ed.*, 2021, **60**, 16661–16667.
14 A. Thomas, J. George, A. Shalabney, M. Dryzhakov, S. J. Varma, J. Moran, T. Chervy, X. Zhong, E. Devaux and C. Genet, *et al.*, *Angew. Chem.*, 2016, **55**, 11462–11466.
15 A. Thomas, L. Lethuillier-Karl, K. Nagarajan, R. M. Vergauwe, J. George, T. Chervy, A. Shalabney, E. Devaux, C. Genet and J. Moran, *et al.*, *Science*, 2019, **363**, 615–619.
16 E. Orgiu, J. George, J. Hutchison, E. Devaux, J. Dayen, B. Doudin, F. Stellacci, C. Genet, J. Schachenmayer and C. Genes, *et al.*, *Nat. Mater.*, 2015, **14**, 1123–1129.
17 E. Eizner, J. Brodeur, F. Barachati, A. Sridharan and S. Kéna-Cohen, *ACS Photonics*, 2018, **5**, 2921–2927.
18 V. C. Nikolis, A. Mischok, B. Siegmund, J. Kublitski, X. Jia, J. Benduhn, U. Hörmann, D. Neher, M. C. Gather and D. Spoltore, *et al.*, *Nat. Commun.*, 2019, **10**, 3706.
19 S. Hou, M. Khatoniar, K. Ding, Y. Qu, A. Napolov, V. M. Menon and S. R. Forrest, *Adv. Mater.*, 2020, **32**, 2002127.
20 M. Gouterman, *J. Mol. Spec.*, 1961, **6**, 138–163.
21 P. G. Savvidis, L. G. Connolly, M. S. Skolnick, D. G. Lidzey and J. J. Baumberg, *Phys. Rev. B: Condens. Matter Mater. Phys.*, 2006, **74**, 113312.
22 A. G. Avramenko and A. S. Rury, *J. Phys. Chem. C*, 2022, **126**, 15776–15787.
23 A. G. Avramenko and A. S. Rury, *J. Phys. Chem. Lett.*, 2020, **11**, 1013–1021.
24 H. Bahsoun, T. Chervy, A. Thomas, K. Börjesson, M. Hertzog, J. George, E. Devaux, C. Genet, J. A. Hutchison and T. W. Ebbesen, *ACS Photonics*, 2018, **5**, 225–232.
25 S. Biswas, M. Mondal, G. Chandrasekharan, K. S. Mony, A. Singh and A. Thomas, *Nat. Commun.*, 2025, **16**, 5115.
26 A. G. Avramenko and A. S. Rury, *J. Chem. Phys.*, 2021, **155**, 064702.
27 D. G. Lidzey, D. D. C. Bradley, M. S. Skolnick, T. Virgili, S. Walker and D. M. Whittaker, *Nature*, 1998, **395**, 53–55.
28 R. E. Blankenship, *Molecular Mechanisms of Photosynthesis*, John Wiley & Sons, 2014.
29 A. Singh, G. Sharma, R. Ghosh, B. P. Singh and P. Vasa, *J. Phys. Chem. C*, 2019, **123**, 16965–16972.
30 Z. Yuan, S.-H. Huang, Z. Qiao, C. Gong, Y. Liao, M. Kim, M. D. Birowosuto, C. Dang, P. C. Wu and Y.-C. Chen, *Laser Photonics Rev.*, 2022, **16**, 2200016.
31 K. Chung, S. Lee, N. Grain, K. Moon, S. Han, S. Yu, H. Kang, D. H. Kim, I. Choi and S. Park, *et al.*, *J. Am. Chem. Soc.*, 2024, **146**, 31150–31158.
32 D. Bajoni, *J. Phys. D: Appl. Phys.*, 2012, **45**, 313001.
33 J. R. Reimers, Z.-L. Cai, R. Kobayashi, M. Rätsep, A. Freiberg and E. Krausz, *Sci. Rep.*, 2013, **3**, 2761.
34 M. Rätsep, J. Linnanto and A. Freiberg, *J. Chem. Phys.*, 2009, **130**, 194501.
35 S. Duan, C. Uragami, K. Horiuchi, K. Hino, X.-F. Wang, S.-I. Sasaki, H. Tamiaki and H. Hashimoto, *Commun. Chem.*, 2021, **4**, 118.
36 K. Kotewicz, S. Tang, L. Edman and E. Wang, *ChemElectroChem*, 2024, **11**, e202300629.
37 A. D. Dunkelberger, R. B. Davidson, W. Ahn, B. S. Simpkins and J. C. Owrutsky, *J. Phys. Chem. A*, 2018, **122**, 965–971.
38 A. B. Grafton, A. D. Dunkelberger, B. S. Simpkins, J. F. Triana, F. J. Hernández, F. Herrera and J. C. Owrutsky, *Nat. Commun.*, 2021, **12**, 214.
39 M. Tavis and F. W. Cummings, *Phys. Rev.*, 1968, **170**, 379.
40 R. J. Holmes and S. R. Forrest, *Phys. Rev. Lett.*, 2004, **93**, 186404.
41 A. Dhavamani, L. Haeberle, J. Wang, S. Kéna-Cohen and M. S. Arnold, *ACS Photonics*, 2021, **8**, 2375–2383.
42 J. Mony, M. Hertzog, K. Kushwaha and K. Börjesson, *J. Phys. Chem. C*, 2018, **122**, 24917–24923.

43 D. M. Coles, N. Somaschi, P. Michetti, C. Clark, P. G. Lagoudakis, P. G. Savvidis and D. G. Lidzey, *Nat. Mater.*, 2014, **13**, 712–719.

44 R. Sáez-Blázquez, J. Feist, A. I. Fernández-Domínguez and F. J. Garca-Vidal, *Phys. Rev. B*, 2018, **97**, 241407.

45 J. A. Ćwik, P. Kirton, S. De Liberato and J. Keeling, *Phys. Rev. A*, 2016, **93**, 033840.

46 F. Herrera and F. C. Spano, *Phys. Rev. Lett.*, 2016, **116**, 238301.

47 S. Takahashi and K. Watanabe, *J. Phys. Chem. Lett.*, 2020, **11**, 1349–1356.

48 M. Son, *Science*, 2025, **389**, 781–782.

49 P. Kinsler and D. M. Whittaker, *Phys. Rev. B: Condens. Matter Mater. Phys.*, 1996, **54**, 4988.

50 W. Ying, M. E. Mondal and P. Huo, *J. Chem. Phys.*, 2024, **161**, 064105.

51 S. T. Wanasinghe, A. Gjoni, W. Burson, C. Majeski, B. Zaslona and A. S. Rury, *J. Phys. Chem. Lett.*, 2024, **15**, 2405–2418.

52 E. O. Odewale, S. T. Wanasinghe and A. S. Rury, *J. Phys. Chem. Lett.*, 2024, **15**, 5705–5713.